

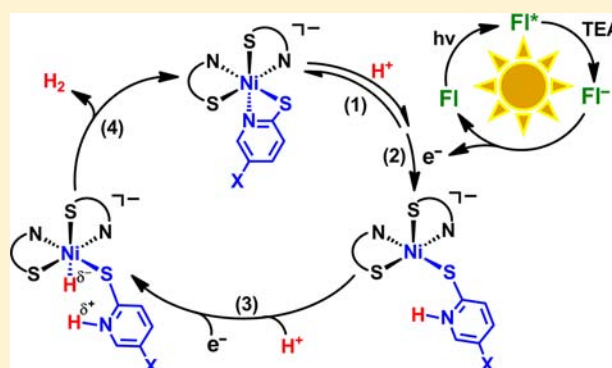
# Nickel Pyridinethiolate Complexes as Catalysts for the Light-Driven Production of Hydrogen from Aqueous Solutions in Noble-Metal-Free Systems

Zhiji Han, Luxi Shen, William W. Brennessel, Patrick L. Holland,\* and Richard Eisenberg\*

Department of Chemistry, University of Rochester, Rochester, New York 14627, United States

**S** Supporting Information

**ABSTRACT:** A series of mononuclear nickel(II) thiolate complexes ( $(\text{Et}_4\text{N})\text{Ni}(\text{X-pyS})_3$  ( $\text{Et}_4\text{N}$  = tetraethylammonium;  $\text{X}$  = 5-H (1a), 5-Cl (1b), 5- $\text{CF}_3$  (1c), 6- $\text{CH}_3$  (1d); pyS = pyridine-2-thiolate),  $\text{Ni}(\text{pySH})_4(\text{NO}_3)_2$  (2),  $(\text{Et}_4\text{N})\text{Ni}(4,6\text{-Y}_2\text{-pymS})_3$  ( $\text{Y}$  = H (3a),  $\text{CH}_3$  (3b); pymS = pyrimidine-2-thiolate), and  $\text{Ni}(4,4'\text{-Z-2,2'-bpy})(\text{pyS})_2$  ( $\text{Z}$  = H (4a),  $\text{CH}_3$  (4b),  $\text{OCH}_3$  (4c); bpy = bipyridine) have been synthesized in high yield and characterized. X-ray diffraction studies show that 2 is square planar, while the other complexes possess tris-chelated distorted-octahedral geometries. All of the complexes are active catalysts for both the photocatalytic and electrocatalytic production of hydrogen in 1/1 EtOH/ $\text{H}_2\text{O}$ . When coupled with fluorescein (Fl) as the photosensitizer (PS) and triethylamine (TEA) as the sacrificial electron donor, these complexes exhibit activity for light-driven hydrogen generation that correlates with ligand electron donor ability. Complex 4c achieves over 7300 turnovers of  $\text{H}_2$  in 30 h, which is among the highest reported for a molecular noble metal-free system. The initial photochemical step is reductive quenching of  $\text{Fl}^*$  by TEA because of the latter's greater concentration. When system concentrations are modified so that oxidative quenching of  $\text{Fl}^*$  by catalyst becomes more dominant, system durability increases, with a system lifetime of over 60 h. System variations and cyclic voltammetry experiments are consistent with a CECE mechanism that is common to electrocatalytic and photocatalytic hydrogen production. This mechanism involves initial protonation of the catalyst followed by reduction and then additional protonation and reduction steps to give a key  $\text{Ni-H}^-/\text{N-H}^+$  intermediate that forms the H-H bond in the turnover-limiting step of the catalytic cycle. A key to the activity of these catalysts is the reversible dechelation and protonation of the pyridine N atoms, which enable an internal heterocoupling of a metal hydride and an N-bound proton to produce  $\text{H}_2$ .



## INTRODUCTION

The splitting of water into its constituent elements to produce  $\text{H}_2$  as a clean, non-carbon-containing fuel and  $\text{O}_2$  as the oxidation product represents a promising way to store and convert solar energy in chemical bonds.<sup>1–3</sup> In such an artificial photosynthetic (AP) scheme, the reductive side of water splitting is the light-driven generation of hydrogen from aqueous protons. A major challenge is finding noble-metal-free catalysts and combining them with highly absorbing photosensitizers (PS) into a robust system for efficient proton reduction into  $\text{H}_2$ .<sup>4,5</sup> In schemes for the proton reduction half-reaction, electrons are provided chemically by a sacrificial reductant in a manner that allows the steps leading to hydrogen generation to be delineated and studied in detail. The sacrificial electron donor in the homogeneous system thus replaces the oxidative side of a complete AP scheme, enabling simpler optimization of proton reduction.

Great progress has been achieved over the last 5 years in the design, synthesis, and study of new catalysts for photochemically driven proton reduction.<sup>6–11</sup> For example, cobaloxime catalysts when coupled with a variety of PS have been found to

generate hydrogen using visible light.<sup>12–18</sup> However, these systems are relatively short-lived (<6 h) and may exhibit low catalytic turnover numbers (TON) (<400 without extra ligand). For the cobaloxime-containing systems, these problems arise from conversion of the catalyst to an inactive form, possibly by ligand decomposition or hydrogenation,<sup>18</sup> and from ligand exchange reactions that occur when the Co ion traverses oxidation states in which the ligands are labile.<sup>19</sup> Nickel(II) bis(diphosphine) complexes, which were originally found to be effective *electrocatalysts* for proton reduction by DuBois and co-workers,<sup>20–22</sup> are also durable catalysts for *photocatalytic* hydrogen generation, although they exhibit relatively low turnover frequencies (TOF) (<20  $\text{h}^{-1}$ ).<sup>23</sup> A nickel 2-mercaptoethanol complex was found by Rong and co-workers to be an active catalyst with a quantum efficiency as high as 12.3% at 460 nm (based on one photon per  $\text{H}_2$  molecule).<sup>24</sup> However, the TON of this catalyst is lower than 100. In more recent work from our laboratories, systems containing cobalt

Received: May 24, 2013

Published: September 4, 2013

bis(dithiolene) complexes as catalysts exhibit up to 9000 TON and a TOF of  $3400 \text{ h}^{-1}$ .<sup>25,26</sup> A TON of 4400 was found recently using a pentadentate polypyridine cobalt catalyst in aqueous media.<sup>27</sup> Another cobalt pentapyridine electrocatalyst from Long and Chang<sup>28</sup> was found to generate hydrogen photochemically at neutral pH in water with a TON of  $\sim 100$ .<sup>29</sup> Many other homogeneous systems use a photosensitizer containing a rare platinum-group element, but still most activity is lost within 10 h of irradiation.<sup>6</sup>

In another recent study, we reported a robust noble-metal-free system using a nickel pyridinethiolate catalyst (**1a**; Figure 1) with a fluorescein (Fl) photosensitizer, and this system

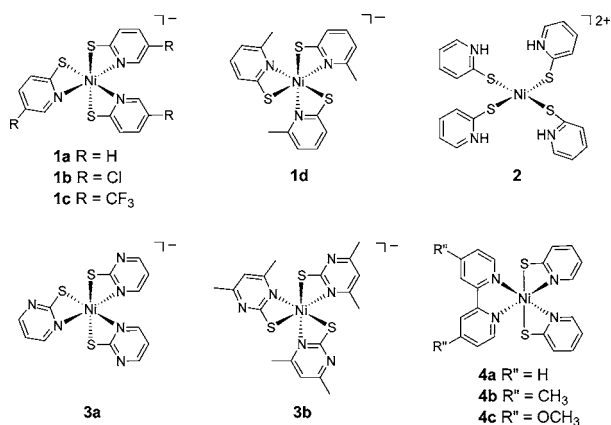


**Figure 1.** Nickel thiolate complexes. In anionic complexes, the counteranion is Et<sub>4</sub>N<sup>+</sup>; in cationic complexes, the counteranion is NO<sub>3</sub><sup>-</sup>.

achieved over 5000 TON when coupled with triethylamine (TEA) as the sacrificial electron donor.<sup>30</sup> This catalyst has a bioinspired aspect, because the nickel ion has mixed N/S ligation as found in the nickel–iron hydrogenases.<sup>31–33</sup> Chen and co-workers later found that binuclear nickel 2-mercaptobenzimidazole and 2-mercaptobenzothiazole complexes gave TON values of 320 when using Fl as photosensitizer.<sup>34</sup> In this paper, we report a series of nine related nickel thiolate complexes and study their activities for both *photocatalytic* and *electrocatalytic* proton reduction. The photochemical pathway for hydrogen generation has been found to proceed by initial reductive quenching of the excited photosensitizer (PS\*). The relative activities of the catalysts, their electrochemical behaviors, and NMR spectroscopic results give insight into the mechanisms of the catalytic processes. Overall, these studies are significant because they show mechanistic detail and trends that will guide continued photocatalyst and electrocatalyst innovations for solar energy utilization.

## RESULTS

**Synthesis and NMR and Electronic Absorption Spectra of the Nickel Thiolate Complexes.** Complexes **1b–d**, **2**, and **3a,b** were synthesized by adding 3–4 equiv of the corresponding thiol to the nickel precursor (Ni(NO<sub>3</sub>)<sub>2</sub> or (Et<sub>4</sub>N)<sub>2</sub>[NiCl<sub>4</sub>]) under N<sub>2</sub>.<sup>35</sup> For complexes **4a–c**, formation of the complex was achieved by slow addition of the corresponding 2,2'-bpy derivative, followed by 2 equiv of the ligand as its thiol (pySH) to give air-stable complexes with crystallized yields of 49–93%. The <sup>1</sup>H NMR spectra of paramagnetic complexes **1**, **3**, and **4** show broad proton resonances ranging from  $\delta$  –11 to 140 ppm, while complex **2**

exhibits sharp, well-defined peaks in the aromatic region consistent with diamagnetism (see Figures S1–S10, Supporting Information). On the other hand, the magnetic moment for complex **3b** (as determined by the Evans method<sup>36</sup>) is  $3.0 \pm 0.2 \mu_B$ , which is consistent with octahedral Ni(II) ( $S = 1$ ).

The UV–vis absorption spectra of the green complexes **1a–d**, **2**, and **3a,b** and the brown-orange complexes **4a–c** were measured at room temperature in MeCN (see Table 1 for data

**Table 1.** Electronic Absorptions for Complexes **1a–d**, **2**, **3a,b**, and **4a–c** in Acetonitrile

complex	$\lambda_{\text{max}}$ nm ( $\epsilon$ , M <sup>-1</sup> cm <sup>-1</sup> )
<b>1a</b> <sup>a</sup>	623 (36), 287 (37900)
<b>1b</b>	625 (34), 293 (39600)
<b>1c</b>	623 (40), 298 (43500)
<b>1d</b>	689 (22), 237 (21300)
<b>2</b>	634 (28), 371 (32700), 291 (82500)
<b>3a</b>	611 (47), 285 (36800)
<b>3b</b>	665 (33), 269 (38800)
<b>4a</b>	283 (29200)
<b>4b</b>	284 (32600)
<b>4c</b>	282 (32900)

<sup>a</sup>From ref 35.

and Figures S11–S14 (Supporting Information) for spectra). Complexes **1a–d**, **2**, and **3a,b** all exhibit a broad low-energy band with a maximum between 610 and 690 nm having a molar absorption coefficient  $\epsilon$  under  $50 \text{ L mol}^{-1} \text{ cm}^{-1}$ , which corresponds to a spin-allowed d–d transition of pseudooctahedral Ni(II).<sup>35,37</sup> Complexes **1a–c** have this band at  $\sim 623$  nm, while the band shifts to 689 nm for complex **1d**. A similar shift from 611 to 665 nm is also observed for complexes **3a,b**. Complexes **1a–d**, **2**, **3a,b**, and **4a–c** all exhibit high-energy bands in the UV region with  $\epsilon$  values on the order of  $10^4 \text{ L mol}^{-1} \text{ cm}^{-1}$ , corresponding to spin-allowed intraligand ( $\pi$ – $\pi^*$ ) transitions.<sup>35</sup>

**Structural Studies.** The solid-state molecular structures of **1b–d**, **2**, **3a,b**, and **4a–c** were determined by single-crystal X-ray crystallography (see Figure 2 and the Supporting Information), and selected bond lengths and angles are given in Tables 2–9, respectively. Complex **2** possesses a square-planar geometry, as expected from the diamagnetism. In the structure, the four pySH ligands coordinate to Ni through the thiolate donors, and the pyridine nitrogen atoms of each ligand are protonated and uncoordinated. NH...O hydrogen bonding between the pySH ligand and NO<sub>3</sub><sup>-</sup> counteranion is also observed (see the Supporting Information), but no NH–S hydrogen bonding. All of the other complexes have pseudo-octahedral geometries that are distorted as a consequence of four-membered  $\kappa^2\text{N,S}$ -chelate rings. In the solid-state structures, complexes **1a,b** and **3a** are found as the *mer* isomers, whereas complexes **1d** and **3b** (which have methyl groups next to the coordinated pyridyl nitrogen atoms) have a *fac* arrangement of the donor N and S atoms. The bond angles in all of these complexes are essentially the same for different pyridinethiolate and pyrimidinethiolate ligands. The four-membered N,S-chelate rings have a N–Ni–S bond angle of  $\sim 68^\circ$ , while for the five-membered N,N-chelate ring involving bipyridine ligands the bite angle is  $\sim 78^\circ$ . For complex **1d** relative to **1a**, the Ni–S bond distance is shortened by  $\sim 0.04 \text{ \AA}$  and the corresponding Ni–N bond distance is lengthened by  $\sim 0.05 \text{ \AA}$  as a consequence of the pyS ligand having a methyl

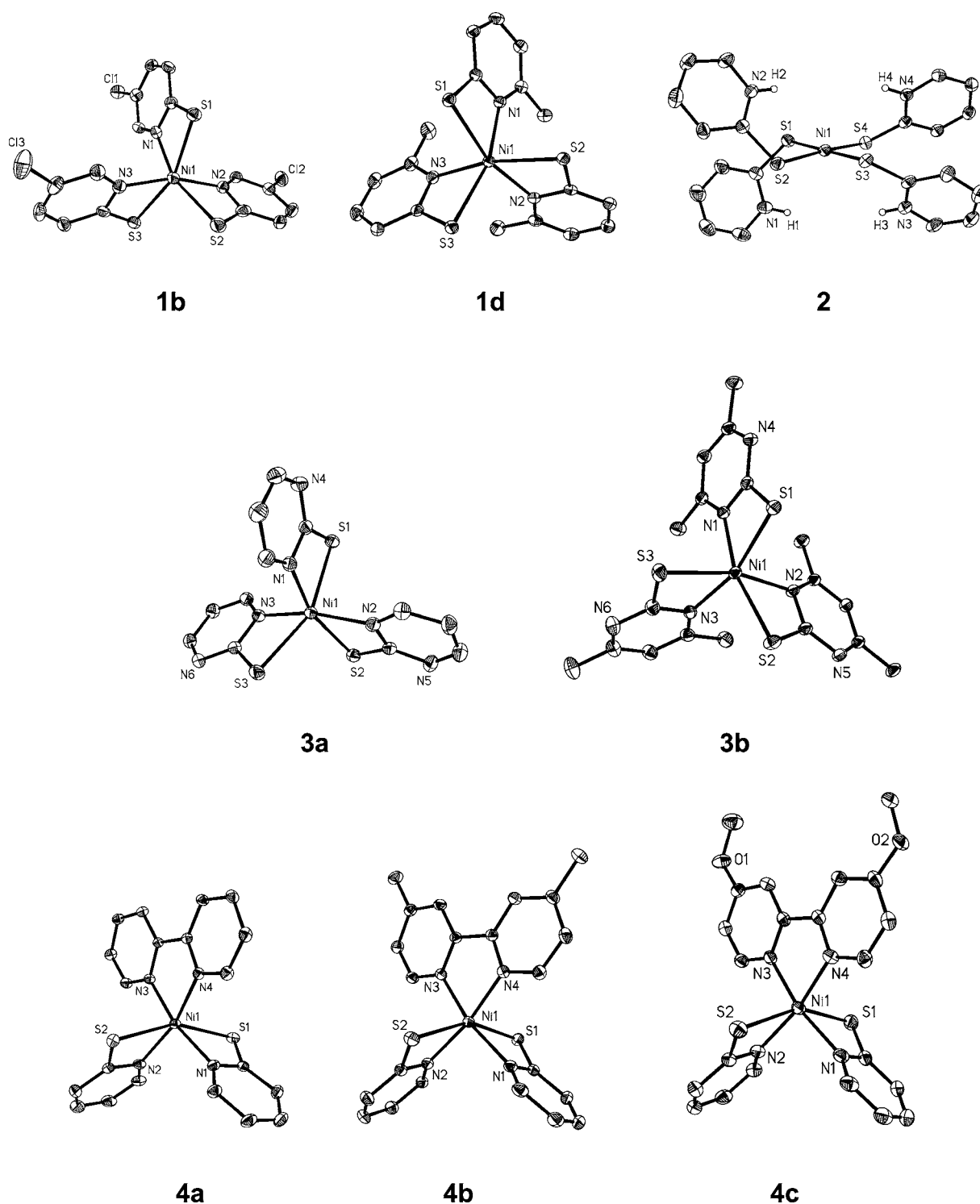


**Figure 2.** X-ray crystal structure diagrams of selected nickel complexes. The hydrogen atoms (except key H atoms for **2**), counterions, and noncoordinating solvent molecules are omitted for clarity. Ellipsoids are plotted at the 50% confidence level.

group at the 6-position of the py ring. A similar trend is observed for complexes **3a,b**. Each of these structural differences is attributed to the steric hindrance of the methyl group cis to the N donor. The square-planar complex **2** has significantly shorter (by 0.25 Å) Ni–S bond lengths relative to the distorted-octahedral complexes. For complexes **4a–c**, the Ni–N and Ni–S (N and S both on pyS ligand) distances are indistinguishable across the series, whereas the Ni–N bpy distances become shorter by ~0.03 Å in going from **4a** to **4c**.

**Photocatalytic Hydrogen Production.** A series of photocatalytic experiments using complexes **1a–d**, **2**, **3a,b**, and **4a–c** for hydrogen production were performed using a solution of TEA (0.36 M) as the sacrificial donor, FI (2.0 mM) as the photosensitizer, and the nickel complex (4.0 μM) as the H<sub>2</sub>-generating catalyst in EtOH/H<sub>2</sub>O (1/1) with a green-light-emitting diode (LED; λ 520 nm, 13 mW/cm<sup>2</sup>) at 15 °C. The amount of H<sub>2</sub> produced was monitored in real time by the pressure change in the reaction vessel and quantified at the end

Table 2. Key Distances and Angles in 1b

Bond Distances (Å)			
Ni(1)–S(1)	2.4983(15)	Ni(1)–N(1)	2.059(4)
Ni(1)–S(2)	2.4909(16)	Ni(1)–N(2)	2.040(4)
Ni(1)–S(3)	2.5019(15)	Ni(1)–N(3)	2.038(4)
Bond Angles (deg)			
S(1)–Ni(1)–N(1)	68.02(12)	S(3)–Ni(1)–N(3)	68.43(13)
S(2)–Ni(1)–N(2)	68.37(13)		

Table 3. Key Distances and Angles in 1d

Bond Distances (Å)			
Ni(1)–S(1)	2.4545(6)	Ni(1)–N(1)	2.1069(17)
Ni(1)–S(2)	2.4698(6)	Ni(1)–N(2)	2.1088(17)
Ni(1)–S(3)	2.4718(6)	Ni(1)–N(3)	2.1145(17)
Bond Angles (deg)			
S(1)–Ni(1)–N(1)	68.39(5)	S(3)–Ni(1)–N(3)	68.62(5)
S(2)–Ni(1)–N(2)	68.16(5)		

Table 4. Key Distances and Angles in 2

Bond Distances (Å)			
Ni(1)–S(1)	2.2134(8)	Ni(1)–S(3)	2.2142(8)
Ni(1)–S(2)	2.2154(8)	Ni(1)–S(4)	2.2036(8)
Bond Angles (deg)			
S(1)–Ni(1)–S(2)	94.15(3)	S(3)–Ni(1)–S(4)	97.82(3)
S(2)–Ni(1)–S(3)	84.45(3)	S(4)–Ni(1)–S(1)	83.67(3)

Table 5. Key Distances and Angles in 3a

Bond Distances (Å)			
Ni(1)–S(1)	2.5002(5)	Ni(1)–N(1)	2.0533(12)
Ni(1)–S(2)	2.4145(5)	Ni(1)–N(2)	2.0755(12)
Ni(1)–S(3)	2.5220(5)	Ni(1)–N(3)	2.0381(12)
Bond Angles (deg)			
S(1)–Ni(1)–N(1)	68.08(4)	S(3)–Ni(1)–N(3)	67.71(4)
S(2)–Ni(1)–N(2)	69.16(4)		

Table 6. Key Distances and Angles in 3b

Bond Distances (Å)			
Ni(1)–S(1)	2.4670(5)	Ni(1)–N(1)	2.0817(14)
Ni(1)–S(2)	2.4553(5)	Ni(1)–N(2)	2.1142(14)
Ni(1)–S(3)	2.4368(5)	Ni(1)–N(3)	2.1020(16)
Bond Angles (deg)			
S(1)–Ni(1)–N(1)	68.20(4)	S(3)–Ni(1)–N(3)	68.78(4)
S(2)–Ni(1)–N(2)	68.28(4)		

Table 7. Key Distances and Angles in 4a

Bond Distances (Å)			
Ni(1)–S(1)	2.5516(7)	Ni(1)–N(2)	2.0594(15)
Ni(1)–S(2)	2.5036(6)	Ni(1)–N(3)	2.0802(15)
Ni(1)–N(1)	2.0418(15)	Ni(1)–N(4)	2.0693(15)
Bond Angles (deg)			
S(1)–Ni(1)–N(1)	67.26(5)	N(3)–Ni(1)–N(4)	78.71(6)
S(2)–Ni(1)–N(2)	68.43(5)		

of the photolysis by GC analysis of the headspace gases. The TON and TOF values for hydrogen production for the different complexes are given in Table 10. Omission of any of the three components leads to no significant H<sub>2</sub> production.

Table 8. Key Distances and Angles in 4b

Bond Distances (Å)			
Ni(1)–S(1)	2.4801(5)	Ni(1)–N(2)	2.0457(13)
Ni(1)–S(2)	2.5300(5)	Ni(1)–N(3)	2.0635(13)
Ni(1)–N(1)	2.0553(13)	Ni(1)–N(4)	2.0699(13)
Bond Angles (deg)			
S(1)–Ni(1)–N(1)	68.53(4)	N(3)–Ni(1)–N(4)	78.86(5)
S(2)–Ni(1)–N(2)	67.91(4)		

Table 9. Key Distances and Angles in 4c

Bond Distances (Å)			
Ni(1)–S(1)	2.4814(9)	Ni(1)–N(2)	2.052(3)
Ni(1)–S(2)	2.5400(9)	Ni(1)–N(3)	2.050(3)
Ni(1)–N(1)	2.058(3)	Ni(1)–N(4)	2.064(3)
Bond Angles (deg)			
S(1)–Ni(1)–N(1)	68.51(8)	N(3)–Ni(1)–N(4)	78.31(10)
S(2)–Ni(1)–N(2)	67.66(8)		

Table 10. Photocatalytic and Electrocatalytic Hydrogen Production and <sup>1</sup>Fl\* Quenching Data for Complexes 1a–d, 2, 3a,b, and 4a–c

complex	TON(30 h)	initial TOF, h <sup>-1</sup>	$E(i_{\text{ps}})$ , V <sub>ps</sub>	$E(i_{\text{qs}})$ , V <sub>ps</sub>	$k_{\text{q}}$ , M <sup>-1</sup> s <sup>-1</sup>
1a	3750 ± 300	258 ± 21	-1.18	-1.61	5.85 × 10 <sup>9</sup>
1b	3420 ± 274	220 ± 18	-1.32	-1.70	9.36 × 10 <sup>9</sup>
1c	2282 ± 160	160 ± 11	-1.32	-1.71	9.38 × 10 <sup>9</sup>
1d	5020 ± 450	371 ± 33	-1.26	-1.61	1.26 × 10 <sup>10</sup>
2	3520 ± 281	191 ± 15	-1.33	-1.56	
3a	1660 ± 158	103 ± 11	-1.00	-1.64	1.21 × 10 <sup>10</sup>
3b	3730 ± 317	251 ± 21	-1.26	-1.67	5.16 × 10 <sup>9</sup>
4a	3095 ± 250	168 ± 14	-1.36 <sup>c</sup>	-1.58	3.87 × 10 <sup>10</sup>
4b	4297 ± 322	265 ± 20	-1.44 <sup>c</sup>	-1.69	2.50 × 10 <sup>10</sup>
4c	7335 ± 645	312 ± 35	-1.46 <sup>c</sup>	-1.70	1.72 × 10 <sup>10</sup>

<sup>a</sup>In 1/1 EtOH/H<sub>2</sub>O (vs SCE). <sup>b</sup>In 8/1/1 DMF/EtOH/H<sub>2</sub>O (vs SCE). <sup>c</sup>In 1/1 MeOH/H<sub>2</sub>O (vs SCE).

The activity of each catalyst system was unaffected when ~1 mL of Hg was added to the system and maintained throughout the photolysis process. This result suggests that colloid formation is not the basis for catalysis.

Figure 3 shows the photolysis results for the tris-(pyridylthiolate) complexes 1a–d under the same experimental conditions. Similar plots for the other complexes are given in the Supporting Information. For the results of Figure 3, the TOF and TON values both increase in the order 1c < 1b < 1a < 1d. The basis of this ordering is discussed further below. The tris(pyridinethiolate) nickel complex 1a has essentially the same activity as the square planar tetrakis(pyridinethiolate) complex 2, in which the uncoordinated pyridyl N-donors are protonated (see Table 10 and Figure S15 (Supporting Information)). This suggests that the pyridinethiolate ligands in 2 are labile, enabling 2 to convert to 1a under the catalytic conditions. Additionally, under the basic conditions of the photolysis, it is likely that proton dissociation from 2 occurs, since TEA is a stronger base than pyridine. Quantum yield determinations were carried out for 1a,d and found to be 4.5 ± 0.7% and 6.0 ± 0.8%, respectively, at 520 nm on the basis of one photon per H<sub>2</sub> molecule (the electron donor TEA decomposes on initial oxidation with the generation of a

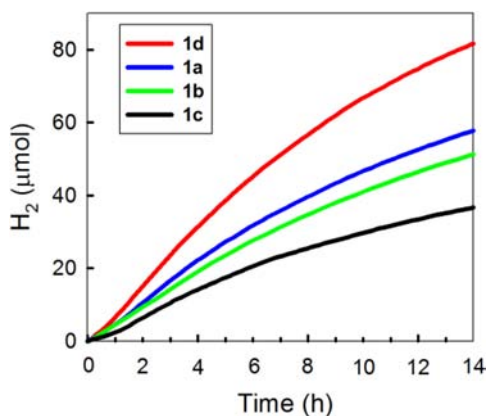


**Figure 3.** Hydrogen production from systems containing nickel complexes **1a–d** ( $4.0 \mu\text{M}$ ), FI ( $2.0 \text{ mM}$ ), and TEA ( $0.36 \text{ M}$ ) in EtOH/H<sub>2</sub>O (1/1) at pH 11.6 upon irradiation with a  $\lambda$  520 nm LED ( $13 \text{ mW/cm}^2$ ) at  $15 \text{ }^\circ\text{C}$ .

second reducing electron so that each TEA yields two electrons for the H<sub>2</sub> produced).

The two pyrimidinethiolate nickel complexes **3a,b** also exhibit good activity for H<sub>2</sub> generation (see Table 10 and Figure S16 (Supporting Information)), with the methylated derivative being substantially more active. A similar trend is also observed with the mixed ligand nickel complexes **4a–c** with activity increasing in the order **4a** < **4b** < **4c** (see Table 10 and Figure S17 (Supporting Information)). The substituents on the bipyridine ligands give evidence of electronic effects on reactivity. For example, complex **4c** with the most electron donating substituents (R = OMe) exhibits the highest catalytic activity, achieving 7335 TONs of hydrogen/mol of catalyst after 30 h of irradiation. For comparison, the tris(bipyridyl) nickel complex [Ni(bpy)<sub>3</sub>](PF<sub>6</sub>)<sub>2</sub> exhibits no H<sub>2</sub> production activity under the same conditions (see the Supporting Information), underscoring the importance of the pyridinethiolate ligand.

The ratio of Ni to pyS ligand was also examined in the course of the photochemical studies, as shown in Figure 4. In the absence of pyridinethiolate ligand, Ni(NO<sub>3</sub>)<sub>2</sub> was inactive for the generation of hydrogen. Addition of pySH to the system led

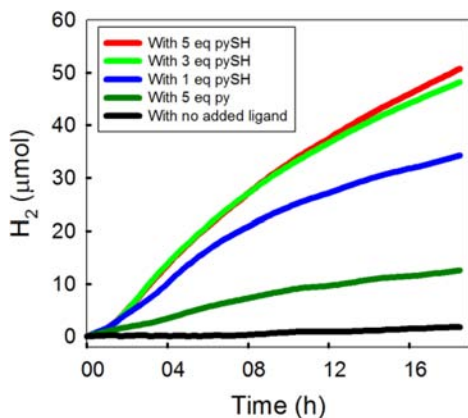


**Figure 4.** Hydrogen production from systems containing Ni(NO<sub>3</sub>)<sub>2</sub> ( $4.0 \mu\text{M}$ ), FI ( $2.0 \text{ mM}$ ), and TEA ( $0.36 \text{ M}$ ) in EtOH/H<sub>2</sub>O (1/1) at pH 11.6 upon irradiation with a  $\lambda$  520 nm LED ( $13 \text{ mW/cm}^2$ ) at  $15 \text{ }^\circ\text{C}$  with no added ligand (black), [py] =  $20 \mu\text{M}$  (dark green), [pyS] =  $4.0 \mu\text{M}$  (blue), [pyS] =  $12 \mu\text{M}$  (green), and [pyS] =  $20 \mu\text{M}$  (red).

to increasing activity up to a maximum of 3 equiv of pyS per Ni(II) ion. Further addition of pySH (giving a ratio of 5/1 ligand/Ni(II)) yielded no greater activity. The addition of pyridine rather than pyridinethiolate led to some activity for H<sub>2</sub> formation, but the turnover number, 420 TON in 16 h, was substantially lower than the activity exhibited by the Ni/pyS system, as shown in Figure 4.

**Electrocatalytic Studies of the Nickel Catalysts.** Cyclic voltammetric experiments were conducted in both aqueous and organic solvent media for complexes **1a–d**, **2**, **3a,b**, and **4a–c**. In dry DMF, no reduction peaks for complexes **1a–c** and **3a,b** were seen at potentials less negative than  $-2 \text{ V}$  (vs SCE), whereas for complexes **1d**, **2**, and **4a–c**, irreversible reduction peaks are seen at  $-1.27$ ,  $-1.33$ ,  $-1.48$ ,  $-1.57$ , and  $-1.61 \text{ V}$ , respectively. However, reduction peaks for all of the complexes are observable when the complex is dissolved in a 1/1 alcohol/H<sub>2</sub>O mixture (Figure 5 for **1a–d**, **2**, and **3a,b** in 1/1 EtOH/H<sub>2</sub>O and Figure 6 for complexes **4a–c** in 1/1 MeOH/H<sub>2</sub>O).

To examine these complexes as potential electrocatalysts for H<sub>2</sub> production, 8 equiv of acetic acid was added to each complex solution and the system was examined by cyclic voltammetry. Significant current enhancement is observed near the onset of the original complex reduction peak for all of the complexes (Figures 5 and 6). A control experiment without the

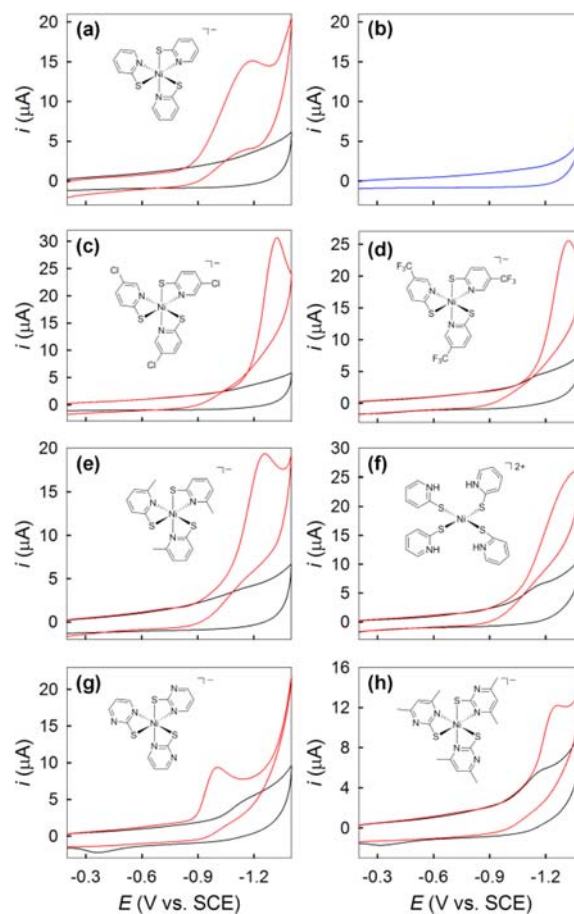


**Figure 5.** Cyclic voltammograms of  $0.1 \text{ mM}$  of catalysts **1a** (a), **1b** (c), **1c** (d), **1d** (e), **2** (f), **3a** (g), and **3b** (h) in 1/1 EtOH/H<sub>2</sub>O without acid (black) and in the presence of  $0.8 \text{ mM}$  acetic acid (red) and a control with  $0.8 \text{ mM}$  acetic acid in the absence of catalyst (b). Conditions:  $0.1 \text{ M KNO}_3$ , glassy carbon as both working and counter electrodes, scan rate  $100 \text{ mV/s}$ .

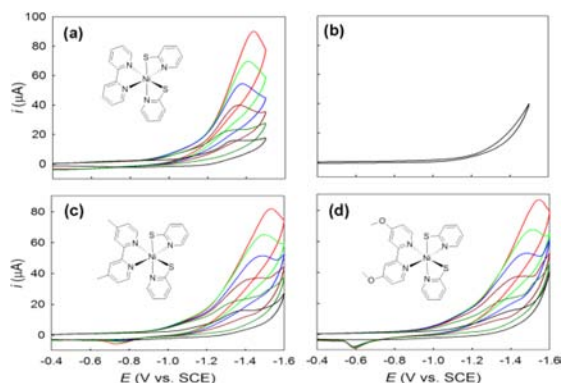


**Figure 6.** Cyclic voltammograms of 0.5 mM of catalysts **4a** (a), **4b** (c), and **4c** (d) in 1/1 MeOH/H<sub>2</sub>O without acid (black) and with [acetic acid] = 1.0 mM (dark green), 2.0 mM (brown), 3.0 mM (blue), 4.0 mM (green), and 5.0 mM (red) and a control with 5.0 mM of acetic acid in the absence of catalyst (b). Conditions: 0.1 M KNO<sub>3</sub>, glassy carbon as both working and counter electrodes, scan rate 100 mV/s.

nickel complex but with the same amount of added acetic acid in the same solvent mixture shows a much lower current enhancement (Figures S5b and 6b). For complexes **4a–c**, which have better solubility and stability in MeOH/H<sub>2</sub>O mixtures, a typical series of voltammograms were obtained with increasing amounts of acetic acid added (Figure 6).

Cyclic voltammetric studies were also carried out on complexes **1a–d**, **2**, **3a,b**, and **4a–c** in an 8/1/1 DMF/EtOH/H<sub>2</sub>O mixture as a function of acid concentration with sequential additions of acetic acid (Figure 7 for **1d** and Figures

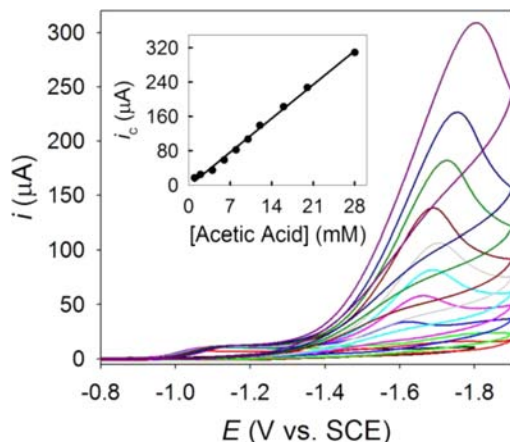


**Figure 7.** Cyclic voltammograms of 1.0 mM of catalyst **1d** in 8/1/1 DMF/EtOH/H<sub>2</sub>O without the presence of acid (black) and in the presence of acetic acid with increasing concentration (other colors). Inset: plot of  $i_c$  taken from the peak plateau versus [acetic acid]. Conditions: 0.1 M TBAPF<sub>6</sub>, glassy carbon as both working and counter electrodes, scan rate 100 mV/s.

S18–S26 (Supporting Information) for other complexes). For all of these complexes, a new reduction wave is observed upon addition of 1 equiv of acid between  $-1.0$  and  $-1.2$  V (vs SCE), which is more positive (less cathodic) than the catalytic wave. However, this wave does not show any catalytic feature upon further addition of acid and disappears after neutralization with TEA (Figures S27 and 28 (Supporting Information)). The observed catalytic current ( $i_c$ ) has a linear correlation with respect to added acetic acid concentration at a scan rate of 0.1

V/s. The observed  $i_c$  feature in the 8/1/1 DMF/EtOH/H<sub>2</sub>O mixed solvent is  $\sim 400$  mV more negative than the corresponding  $i_c$  value found in systems having the 1/1 alcohol/H<sub>2</sub>O mixed solvent (Table 10).

#### Fluorescence Quenching of Fl\* by Nickel Catalysts.

The photochemically driven electron-transfer steps were studied through <sup>1</sup>Fl\* quenching by complexes **1a–d**, **2**, **3a,b**, and **4a–c** in 1/1/8 EtOH/H<sub>2</sub>O/DMF solvent mixtures at pH 11.6 (DMF used for higher solubility of the nickel complexes; the quenching rate constant was found to be independent of the ratio of the solvent components<sup>30</sup>). The fluorescence of Fl\* (excited at 460 nm) is quenched by all of the nickel complexes following linear Stern–Volmer behavior with near-diffusion-controlled rates on the order of  $10^{10}$  M<sup>-1</sup> s<sup>-1</sup> (Table 10 for quenching rates and Figures S29–S37 (Supporting Information) for the linear plots).

<sup>1</sup>H NMR Studies on Catalyst Protonation. To study the protonation of the nickel complexes, <sup>1</sup>H NMR spectra were recorded in *d*<sub>6</sub>-DMSO with the addition of acid. The paramagnetically shifted spectra of **1d** show that the four proton peaks of the complex shift significantly upon addition of 1 equiv of trifluoroacetic acid (Figure S38 (Supporting Information)) and that the change is reversible. The addition of TEA as a base leads to complete recovery of the initial resonances. The protonation/deprotonation also correlates with the observed color change from green to orange and back to green. A similar result for complex **1a** was also observed (Figure S39 (Supporting Information)).

## DISCUSSION

**Initial Photochemical Steps.** In an earlier report of the complex (NEt<sub>4</sub>)[Ni(pyS)<sub>3</sub>] (**1**) as the catalyst for H<sub>2</sub> generation in a system containing Fl as the photosensitizer and TEA as the sacrificial electron donor, mechanistic proposals were presented regarding the initial photochemical steps and subsequent electron and proton transfers leading to H<sub>2</sub> formation.<sup>30</sup> The present discussion expands on that analysis to include the additional mechanistic data described here.

With regard to the initial photochemical step, electron transfer quenching of Fl\* by either TEA (reductive quenching to form Fl<sup>-</sup> + TEA<sup>+</sup>) or Ni catalyst (presumably oxidative quenching to form Fl<sup>+</sup> + Ni catalyst<sup>-</sup>) is possible, but the relative concentrations of sacrificial donor and Ni catalyst determine the primary photochemical path followed upon irradiation. The rate constant for the reductive quenching by TEA has been reported previously by us to be  $5.5 \times 10^7$  M<sup>-1</sup> s<sup>-1</sup>.<sup>30</sup> For all of the Ni complexes reported here (**1a–d**, **2**, **3a,b**, and **4a–c**), the <sup>1</sup>Fl\* quenching rate constants ( $k_q$ ) were determined from linear fits of the Stern–Volmer equation (Table 10). These quenching rate constants are near the diffusion-controlled limit and range from  $5.8 \times 10^9$  to  $3.9 \times 10^{10}$  M<sup>-1</sup> s<sup>-1</sup>. However, even though the quenching rate constants by the Ni catalysts are 2–3 orders of magnitude greater than the reductive quenching rate constant by TEA, the primary electron-transfer quenching path from the <sup>1</sup>Fl\* excited state is via reaction with TEA, since the electron donor's concentration (0.36 M) is  $\sim 10^5$  times greater than that of the Ni catalyst ( $4 \times 10^{-6}$  M) employed in the system.

The subsequent electron transfer from Fl<sup>-</sup> to the catalyst was also critical for the effectiveness and durability of the system. The prior report of the Fl/**1a**/TEA system found that if the catalyst was not present for reduction by Fl<sup>-</sup>, the dye decomposed rapidly (within 20–30 min).<sup>30</sup> With catalyst

present, the major FI absorption lasted for many hours, consistent with rapid electron transfer from  $PS^*$  relative to  $PS^-$  decomposition.

The reductive quenching pathway involving  $PS^*$  and the electron donor, and the subsequent electron transfer from  $PS^-$  to the catalyst, have been described in other reported three-component homogeneous photocatalytic systems for  $H_2$  generation.<sup>6</sup> In those systems, the organic PS was either Eosin Y or chalcogen-substituted rhodamine dyes<sup>16,30</sup> with a long-lived  $^3\pi\pi^*$  excited state, and the catalyst was a cobaloxime derivative. In those systems, the dye bleached within minutes under irradiation in the presence of the sacrificial donor without any catalyst present. However, addition of catalyst greatly prolonged the durability of the PS by allowing electron transfer from  $PS^-$  to the catalyst and subsequent proton reduction to  $H_2$ .

To examine this analysis further in the present system, the TEA concentration was reduced to 7.0 mM to slow the reductive quenching rate and determine the potential viability of an oxidative quenching path. Catalyst **4a**, which has the highest quenching rate constant, was used in this experiment at 0.05 mM concentration. In this case, the oxidative quenching rate is calculated from  $k_q[\text{quencher}]$  to be  $\sim 5$  times faster than the reductive quenching rate. After depletion of TEA for  $H_2$  generation, the system was regenerated by adding more TEA, with the system lasting over 60 h (Figure S40 (Supporting Information)). A control experiment using 0.36 M instead of 7.0 mM [TEA] lasted only 15 h.

The result supports the hypothesis that a more stable organic dye containing system for  $H_2$  could be obtained if either (1) the photochemical step of  $PS^*$  involved electron transfer to the catalyst rather than reduction of  $PS^*$  by the electron donor or (2) the reduced dye  $PS^-$  was stable to decomposition. It is also notable that in the present system the quenching of the dye occurred from its  $^1\pi\pi^*$  excited state rather than from the corresponding  $^3\pi\pi^*$  state, indicating that bimolecular quenching can compete with radiative and nonradiative decay for certain dyes. The exploration of new systems containing organic  $PS^*$  that can transfer electrons directly to the catalyst (before reduction by the sacrificial donor) thus seems compelling.

**Mechanism of Catalysis in Proton Reduction.** We have previously proposed a mechanism for proton reduction by the nickel complex in which protonation of the pyS ligand generates the active catalyst, which is subsequently reduced from formally Ni(II) to Ni(I). However, the later steps in the mechanism were less clear. Here, the additional electrochemical studies and substituent effects point toward a CECE mechanism for proton reduction and  $H_2$  formation.

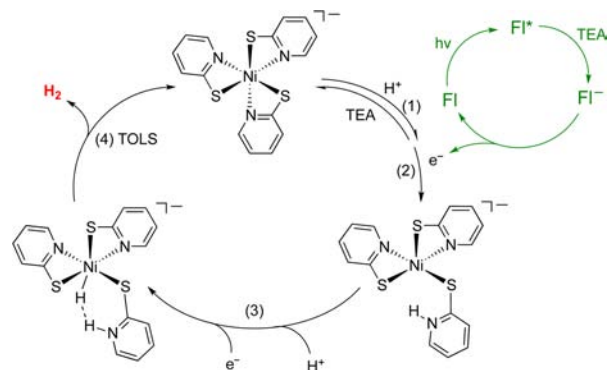
For the nickel complexes **1a–c** and **3a** in 8/1/1 DMF/EtOH/ $H_2O$ , the CV shows no reduction peak at potentials less negative than  $-2.0$  V (vs SCE), indicating that the complexes cannot accept an electron from  $^1FI^*$  in this solvent mixture. However, upon addition of acetic acid to the nickel complexes **1a–c** and **3a**, two reduction peaks are observed in the voltammogram (Supporting Information). There is no catalytic wave observed for the peak at the more positive potential. We tentatively assign this peak to a “Ni(II)–H”/“Ni(I)–H” couple formed in situ through protonation of the original complexes. Despite the use of the “Ni(II)–H”/“Ni(I)–H” designation for this couple, the site of protonation is not specified at this point but is discussed further below.

Even though complexes **1d**, **3b**, and **4a–c** show an irreversible reduction wave before addition of acid, a new wave at slightly more positive potential is observed upon addition of 1 equiv of acid (Supporting Information). This wave is at a potential similar to the proposed “Ni(II)–H”/“Ni(I)–H” couple of complexes **1a–c** and **3a**. For the protonated complex **2**, an irreversible reduction wave is seen in the absence of acid and remains essentially unchanged upon the addition of acid (a slight shift to more a positive potential may be due to a change of pH).

For all of the complexes the catalytic wave appears more negative of the first reduction wave. This observation is consistent with the need for protonation of the catalysts (except for **2**, which is already protonated) for reduction to occur followed by an additional protonation and reduction for hydrogen production.

To examine this hypothesis further in more aqueous media, CVs were recorded in a 1/1 alcohol/ $H_2O$  mixture at 0.1 mM catalyst concentration (Figures 5 and 6). In each case, an irreversible reduction peak was observed in the absence of acid. A catalytic wave grew in for each of the complexes upon addition of 8 equiv of acetic acid, indicating that they are active proton reduction catalysts in this solvent. The color change from green (in DMF) to orange (in 1/1 alcohol/ $H_2O$ ) for complexes **1a–d** and **3a,b** is associated with their initial protonation of the complexes, as indicated in step 1 of Scheme 1. This protonation step was supported further by  $^1H$  NMR

#### Scheme 1. Proposed Mechanism of Hydrogen Formation<sup>a</sup>



<sup>a</sup>The reversibility of the steps in the scheme beyond the initial protonation has not been established. TOLS = turnover-limiting step.

spectroscopy of complexes **1a,d** (Figure 7 and Supporting Information). Addition of 1 equiv of trifluoroacetic acid to each complex gave rise to new paramagnetically shifted resonances, while addition of TEA as a base returned each sample back to its original spectrum. Thus, the protonation of these complexes is reversible.

The site of protonation suggested in Scheme 1 on nickel complexes **1a–d**, **3a,b**, and **4a** as the pyridyl N with ligand dechelation is a matter of conjecture. Although isolation of the orange protonated species indicated above was not successful, the structure of **2** obtained with 4 equiv of protonated pyS ligand clearly shows that the dechelation of each ligand was associated with the protonation of each pyridyl N. As noted above, complex **2** has photocatalytic activity for hydrogen production identical with that of **1a** (Supporting Information), which suggests similar intermediates are formed during catalysis starting from both complexes. Importantly, we found that

complex **2** can be converted into **1a** by addition of NaOH as base in MeOH. This process was observed by  $^1\text{H}$  NMR spectroscopy, and only **1a** as the product was observed (see the Supporting Information). In the structure of **2**, the four pyridyl rings are bent toward the nickel center and the distances between the proton (on the pyridine N atom) and the Ni(II) ion range from 2.86 to 3.08 Å, which is slightly shorter than the 3.32 Å reported for the Fe(II)⋯H–N distance in an [Fe–Fe] hydrogenase mimic.<sup>38</sup> Thus, it is proposed that the site of initial protonation in these complexes is the pyridyl N with dechelation and that proton transfer from this ligand is important for H<sub>2</sub> generation.

We have noted that, with further addition of acetic acid, a catalytic wave is seen at a *more* negative potential than the “Ni(II)–H”/“Ni(I)–H” couple. This observation is consistent with the proposed mechanism involving further reduction of the initial “Ni(I)–H” intermediate for hydrogen production. The catalytic peak current follows a linear correlation with respect to [acetic acid] for all these complexes (Figure 7 and Supporting Information), indicating the reaction rate has a second-order dependence on [H<sup>+</sup>].<sup>39</sup> This implies that the second protonation step occurs at or before the turnover-limiting step (Scheme 1, step 3). The second reduction, at which the catalytic current is seen, leads to formation of a proposed Ni hydride intermediate. In the photochemical reaction, the electron for this reduction is supplied by a second F<sup>–</sup> or by the decomposition of TEA.

Structural support for the proposed hydride intermediate in Scheme 1 and the role of pyridinethiolate as a proton shuttle comes from work by Morris and co-workers, who described an Ir(pyS) complex that undergoes heterolytic splitting of dihydrogen to form a metal hydride and protonated pyS.<sup>40</sup> In the case of the IrH(pySH) complex heterolytic activation of H<sub>2</sub> is preferred, whereas in the case of the Ni(pyS) complexes, H<sub>2</sub> evolution is preferred, probably from differences in the M–H bond energies (BDE(Ir–H) > (BDE(Ni–H))).

The coordination modes of the pyS ligand on Ni seen in the structures of the tris(pyridinethiolate) Ni complexes and the square-planar complex **2** are consistent with computational studies of ligand protonation and dechelation.<sup>41</sup> Dechelation to generate a pendent nitrogen base for proton acceptance and delivery to the metal center are similar to those proposed for proton reduction/hydrogen oxidation in [Fe–Fe] hydrogenases,<sup>32,42–44</sup> [Fe–Fe] hydrogenase mimics,<sup>38</sup> and some nickel bis(diphosphine) catalysts.<sup>20–22</sup>

The CECE mechanism that is proposed in Scheme 1 for the Ni pyridinethiolate complexes during hydrogen production differs slightly from the ECEC mechanism proposed by Helm and co-workers<sup>45</sup> for Ni bis(diphosphine) complexes, in which the diphosphine has a single pendant amine. The difference in the initial step during catalysis for these two classes of catalysts could be due to the different charges on the complexes. The Ni pyridinethiolate complexes have an overall 1– or 0 charge and thus favor an initial protonation step, while the Ni bis(diphosphine) complexes have an overall 2+ charge and favor reduction first. There is also a difference in turnover-limiting steps: Helm and co-workers found that the turnover-limiting step is the first protonation of the Ni(I) species.<sup>45</sup> The different mechanism from the reported complexes here could be due to the high-spin electronic configuration, which gives more labile ligands and rapid dechelation of the four-membered Ni(pyS) ring, speeding the initial protonation.

In view of the difference in the pH of the photochemical and electrochemical experiments, there may be different degrees of catalyst protonation prior to each reduction step. However, insight into protonation prior to the initial reduction step was obtained by monitoring the UV–vis spectra of complex **1a** in going from pH 11.5 to pH 5.2. Isosbestic points were observed over this range (Figure S42 (Supporting Information)), indicating that over this range only two species are present: the unprotonated complex and the singly protonated complex with one unchelated ligand. Therefore, the simplest interpretation is that the initial CE steps at the catalyst for photochemical and electrochemical H<sub>2</sub> formation are the same. However, further study is needed to determine if differences exist in the rest of the catalytic cycle.

**Ligand Dependence of Catalytic Activity.** The present study also shows the dependence of catalytic activity as a function of ligand electronic factors in light-driven H<sub>2</sub> production. In this study, Ni tris(pyridinethiolate) (**1a–d**), tris(pyrimidinethiolate) (**3a,b**), and bipyridine bis(pyridinethiolate) (**4a–c**) complexes and tetrakis(pyridinethiolate) complex **2** were examined as catalysts for the photo- and electrochemically driven generation of H<sub>2</sub>. For these catalysts under identical photolysis conditions, both the catalyst TON and initial TOF correlate with ligand electron-donating ability. For example, the TON and TOF for **1c**, **3a**, and **4a**, which have electron-withdrawing ligand substituents, are approximately half of the corresponding values for the catalysts **1d**, **3b**, and **4c**, which have electron-donating ligand substituents. A rationalization of these observations is that more electron-donating ligands give a more basic nickel hydride intermediate (Scheme 1) for the heterocoupling of Ni–H<sup>–</sup> and N–H<sup>+</sup> to form H<sub>2</sub>. While the basicity of the py N would also be affected by these ligand substituents, the ligand electronic effects exert a stronger influence on the Ni center. Though this may seem surprising, note that for complexes **4a–c** changing only the bpy ligand electronic effect leads to the same activity trend as for pyridines and has minimal effect on the pyridyl N basicity. The results are thus consistent with the notion that the electron-donating substituents make the reduced Ni more electron rich and that the subsequent hydride intermediate becomes more reactive for heterocoupling with a pyridine-attached proton. On the basis of the ligand electronic effects and second-order dependence of [H<sup>+</sup>] on catalytic rate, the heterocoupling step for hydrogen formation is proposed to be the turnover-limiting step for the catalytic cycle. This is similar to the case for the [Ni(P<sub>2</sub>N<sub>2</sub>)<sub>2</sub>]<sup>2+</sup> complexes of Dubois and co-workers.<sup>46–49</sup> The higher activity observed for **1d** and **3b** relative to **1a–c** and **3a**, respectively, may also be due to the steric influence of the Me substituent that would facilitate dechelation as shown in Scheme 1.

A correlation between the photocatalytic and electrocatalytic activity of the nickel thiolate catalysts for hydrogen generation is also observed. For example, complex **4c** is the most active catalyst for light-driven H<sub>2</sub> generation, and it also has the most cathodic catalytic wave relative to **4b** and **4a** (Table 10). A similar ordering is also observed for complexes **3a,b**. This fits our mechanistic model, because once the catalyst is reduced (step 3 in Scheme 1), the resultant intermediate would have a larger driving force for hydride formation and hence a faster TOF for hydrogen production from heterocoupling of the hydride and proton.

The Ni pyridinethiolate catalyst can also be generated in situ with addition of 3 equiv of the pyS<sup>–</sup> ligand to Ni(NO<sub>3</sub>)<sub>2</sub>.

Control experiments performed with  $\text{Ni}(\text{NO}_3)_2$  or  $[\text{Ni}(\text{bpy})_3] \cdot (\text{PF}_6)_2$  in the system in the absence of an N-donor ligand did not produce significant amounts of hydrogen (Figures 3b and 4). While the addition of 5 equiv of pyridine to  $\text{Ni}(\text{NO}_3)_2$  yielded a system of modest activity (420 TON of  $\text{H}_2$ ), hydrogen-generating activity increased substantially upon the addition of 1 equiv of the  $\text{pyS}^-$  ligand (the ligand is added as  $\text{pySH}$  but is rapidly deprotonated under the basic reaction conditions). The activity of the system reached a maximum at 3 equiv of  $\text{pyS}^-$  ligand (Figure 4), but further addition of ligand led to no further activity increases. The results highlight the importance of using the pyridinethiolate ligand for catalysis and its dual roles in stabilizing the reduced Ni center and providing a means for transferring protons from solution to a suggested hydride intermediate.

## CONCLUSIONS

Several nickel pyridine- and pyrimidinethiolate complexes are active for both light-driven and electrocatalytic hydrogen production in aqueous/organic solvent mixtures. The initial photochemical step is reductive quenching in which the  $\text{Fl}^*$  excited state is reduced by reaction with TEA. This pathway dominates because the relative concentration of TEA is  $10^5$  greater than that of the Ni catalyst. However, an oxidative quenching pathway can be enforced by using low TEA concentration and higher Ni catalyst concentration, leading to a system that is more robust but less active under these conditions.

The catalytic mechanism for  $\text{H}_2$  formation at the nickel ion starts with a protonation of the pyridyl N that is likely to occur with dechelation. The protonated pyridyl N subsequently serves to deliver  $\text{H}^+$  to a proposed Ni hydride intermediate that forms in the cycle for  $\text{H}_2$  generation. The rate-limiting step is proposed to be H–H formation, which is fastest when electron-donating groups are used on the supporting ligands. The highest activity catalyst is **4c**, which exhibits TON and TOF values that are among the highest for molecular noble-metal-free photochemical systems.

## EXPERIMENTAL SECTION

**Materials.** The complexes  $(\text{Et}_4\text{N})[\text{Ni}(\text{pyS})_3]$  (**1a**) and  $[\text{Ni}(\text{bpy})_3] \cdot (\text{FP}_6)_2$  (**5**) were synthesized by previously reported methods and recrystallized from acetonitrile.<sup>35,50</sup> All solvents were used without further purification unless otherwise stated. Pyridine-2-thiol ( $\text{pySH}$ ), 5-Cl-pyridine-2-thiol (5-ClpySH), 5-CF<sub>3</sub>-pyridine-2-thiol (5-CF<sub>3</sub>pySH), 6-CH<sub>3</sub>-pyridine-2-thiol (6-MepySH), pyrimidine-2-thiol (pymSH), 4,6-(CH<sub>3</sub>)<sub>2</sub>-pyrimidine-2-thiol (4,6-dmpymSH), 2,2'-bipyridine (bpy), 4,4'-dimethyl-2,2'-bipyridine (dmbpy), 4,4'-dimethoxy-2,2'-bipyridine (dmobpy), nickel(II) nitrate hexahydrate, nickel(II) chloride hexahydrate, sodium metal, fluorescein (Fl), tetraethylammonium bromide ( $\text{Et}_4\text{NBr}$ ), tetraethylammonium chloride ( $\text{Et}_4\text{NCl}$ ), tetrabutylammonium hexafluorophosphate ( $\text{Bu}_4\text{NPF}_6$ ), and triethylamine (TEA) were purchased from Aldrich and used without further purification.

**Syntheses.** All syntheses of nickel thiolate complexes were performed in Schlenk flasks under an  $\text{N}_2$  atmosphere and using solvents dried with 4 Å molecular sieves. Complexes **1a–d**, **2**, and **3a,b** were stored under  $\text{N}_2$ , and **4a–c** were stored under ambient atmosphere without protection from water and oxygen.

**Spectroscopic Measurements.**  $^1\text{H}$  and  $^{19}\text{F}$  NMR were recorded on a Bruker Avance 400 or 500 MHz spectrometer and are reported in ppm at room temperature.  $^1\text{H}$  NMR spectra were referenced to the residual solvent peak, and  $^{19}\text{F}$  NMR spectra were referenced to trifluorotoluene. UV–vis spectra in acetonitrile were taken on a Cary 60 UV/vis spectrophotometer using a 1 cm path length quartz cuvette.

**$(\text{Et}_4\text{N})[\text{Ni}(5\text{-ClpyS})_3]$  (**1b**).** 5-ClpySH (0.5 g, 3.4 mmol) was added to a solution of sodium methoxide which was prepared by dissolving Na (79 mg, 3.4 mmol) in methanol (5 mL). One equivalent of  $\text{Et}_4\text{NBr}$  (0.72 g, 3.4 mmol) was added afterward. After the mixture was stirred for 1 h, the solvent was removed under vacuum.  $(\text{Et}_4\text{N})5\text{-ClpyS}$  was extracted with 10 mL of acetonitrile and filtered, and a solution containing  $(\text{Et}_4\text{N})_2[\text{NiCl}_4]$  (0.39 g, 0.85 mmol) in 10 mL of acetonitrile was added slowly over 30 min. As the addition of the nickel precursor proceeded, the color of the solution changed from yellow to green with a white precipitate. After the mixture was stirred for 2 h, its volume was reduced to ~10 mL, causing precipitation of the green product. The mixture was then filtered and kept at  $-20^\circ\text{C}$  for 24 h. The green block crystals were collected via suction filtration and dried under vacuum. The crystal yield was 0.22 g (41%) on the basis of  $(\text{Et}_4\text{N})_2[\text{NiCl}_4]$  used.  $^1\text{H}$  NMR ( $\text{CD}_3\text{CN}$ ,  $20^\circ\text{C}$ ):  $\delta$  105, 80, 12.1, 3.2, 1.2 ppm. Anal. Calcd for  $\text{C}_{23}\text{H}_{29}\text{N}_4\text{S}_3\text{Cl}_3\text{Ni}$ : C, 44.36; H, 4.69; N, 9.00. Found: C, 44.64; H, 4.78; N, 9.02.

**$(\text{Et}_4\text{N})[\text{Ni}(5\text{-CF}_3\text{pyS})_3]$  (**1c**).** This complex was prepared in a manner analogous to that described for **1b** except for the purification process. After the green complex was formed and stirred for 2 h, the solvent was removed completely by vacuum. A 65 mL portion of dry diethyl ether was added to extract most of the green complex, while the white precipitate remained insoluble. The solution was filtered and the solvent was removed. The product was allowed to dry overnight under vacuum and collected as a green powder. The yield was 0.22 g (35.6%).  $^{19}\text{F}\{^1\text{H}\}$  NMR ( $\text{CD}_3\text{CN}$ ,  $20^\circ\text{C}$ ):  $\delta$  19.27 (s).  $^1\text{H}$  NMR ( $\text{CD}_3\text{CN}$ ):  $\delta$  104, 68.8, 12.4, 3.2, 1.2 ppm. Anal. Calcd for  $\text{C}_{26}\text{H}_{29}\text{N}_4\text{S}_3\text{F}_9\text{Ni}$ : C, 43.17; H, 4.04; N, 7.74. Found: C, 42.97; H, 4.02; N, 7.41.

**$(\text{Et}_4\text{N})[\text{Ni}(6\text{-MepyS})_3]$  (**1d**).** This complex was prepared in a manner analogous to that described for **1b**. The yield was 0.31 g (65%).  $^1\text{H}$  NMR ( $\text{CD}_3\text{CN}$ ,  $20^\circ\text{C}$ ):  $\delta$  63.6, 54.2, 9.8, 3.2, 1.3,  $-7.7$  ppm. Anal. Calcd for  $\text{C}_{26}\text{H}_{38}\text{N}_4\text{S}_3\text{Ni}$ : C, 55.62; H, 6.82; N, 9.98. Found: C, 55.33; H, 6.86; N, 9.94.

**$[\text{Ni}(\text{HpyS})_4](\text{NO}_3)_2 \cdot \text{EtOH}$  (**2**).** A 0.727 g (2.5 mmol) amount of  $\text{Ni}(\text{NO}_3)_2(\text{H}_2\text{O})_6$  in 5 mL of EtOH was added to a solution containing 1.11 g (10.0 mmol) of  $\text{pySH}$  in 24 mL of EtOH. A dark green precipitate appeared during addition. After 1 h of stirring, the solid product was collected through filtration. A small portion of the product that remained in the filtrate was collected as dark green crystals after keeping the solution at  $-20^\circ\text{C}$  for 10 h. The combined yield was 1.23 g (73%).  $^1\text{H}$  NMR ( $\text{CD}_3\text{OD}$ ,  $20^\circ\text{C}$ ):  $\delta$  7.63 (4H), 7.42 (8H), 6.79 (4H) ppm. Anal. Calcd for  $\text{C}_{20}\text{H}_{20}\text{N}_6\text{S}_4\text{O}_6\text{Ni}$ : C, 38.29; H, 3.21; N, 13.39. Found: C, 38.25; H, 3.25; N, 12.90.

**$(\text{Et}_4\text{N})[\text{Ni}(\text{pymS})_3]$  (**3a**).** PymSH (0.5 g, 4.46 mmol) was added to a solution of potassium *tert*-butoxide (0.5 g, 4.46 mmol) in 5 mL of methanol.  $\text{Et}_4\text{NBr}$  (0.937 g, 4.46 mmol, 1.00 equiv) was added. After the mixture was stirred for 1 h, the solvent was removed under vacuum.  $(\text{Et}_4\text{N})\text{pymS}$  was extracted with 10 mL of acetonitrile and filtered into a solution containing  $\text{Ni}(\text{NO}_3)_2(\text{H}_2\text{O})_6$  (0.37 g, 1.27 mmol) in 15 mL of acetonitrile. The color of the solution changed from blue to green during addition. After 2 h of stirring, the volume of the mixture was reduced to ~12 mL, and to this solution was added 10 mL of diethyl ether to give a white precipitate. The solution was filtered and cooled to  $0^\circ\text{C}$ . Dark green crystals were collected after 24 h. The yield was 0.42 g (63%).  $^1\text{H}$  NMR ( $\text{CD}_3\text{CN}$ ,  $20^\circ\text{C}$ ):  $\delta$  101, 46.3, 15.5, 3.2, 1.2. Anal. Calcd for  $\text{C}_{20}\text{H}_{29}\text{N}_7\text{S}_3\text{Ni}$ : C, 45.98; H, 5.60; N, 18.77. Found: C, 45.95; H, 5.60; N, 18.59.

**$(\text{Et}_4\text{N})[\text{Ni}(4,6\text{-dmpymS})_3] \cdot (\text{Et}_3\text{NHCl})$  (**3b**).** This complex was prepared in a manner analogous to that described for **3a** except for using TEA instead of potassium *tert*-butoxide as base. After the volume of the solution was reduced to ~12 mL, the mixture was stored at  $0^\circ\text{C}$  overnight. Clear crystals formed, and the solution was filtered. Volatile materials were removed from the filtrate to give a crude green product, which was washed with 1/2 acetonitrile/diethyl ether mixture. Green crystals were obtained by recrystallization of the crude product from 1/2 v/v acetonitrile/ether mixture at room temperature. The yield was 0.57 g (60%).  $^1\text{H}$  NMR ( $\text{CD}_3\text{CN}$ ,  $20^\circ\text{C}$ ):  $\delta$  44.3, 3.1, 1.3,  $-7.0$  ppm. Anal. Calcd for  $\text{C}_{32}\text{H}_{57}\text{N}_8\text{S}_3\text{Ni}$ : C, 51.65; H, 7.72; N, 15.06. Found: C, 51.89; H, 7.51; N, 15.12.

**Ni(bpy)(pyS)<sub>2</sub> (4a).** This complex was originally synthesized by a electrochemical method and cocrystallized with the bpy starting ligand.<sup>51</sup> Here, we report a straightforward chemical method that gives pure material with high yield. A solution of 2,2'-bipyridine (1.0 g, 6.4 mmol) in 15 mL of acetonitrile was added slowly to a solution containing Ni(NO<sub>3</sub>)<sub>2</sub>(H<sub>2</sub>O)<sub>6</sub> (1.86 g, 6.4 mmol) in 100 mL of acetonitrile over 30 min. The color of the solution changed from light blue to dark blue. A solution containing pySH (1.42 g, 12.9 mmol) and TEA (2.2 mL, 16.0 mmol) in 50 mL of acetonitrile was then added slowly over 1 h. The solution turned orange, and a yellow precipitate formed after stirring for another 1 h. The product was collected by suction filtration and dissolved in a minimal amount of CH<sub>2</sub>Cl<sub>2</sub>. A layer of hexane was added slowly to the top of the solution. Dark orange needles were collected after 2 days. The yield was 2.4 g (86%). <sup>1</sup>H NMR (CDCl<sub>3</sub>, 20 °C): δ 138, 110, 72, 60.2, 57.5, 43.4, 15.8, 10.6 ppm. Anal. Calcd for C<sub>20</sub>H<sub>16</sub>N<sub>4</sub>S<sub>2</sub>Ni·0.5H<sub>2</sub>O: C, 54.09; H, 3.63; N, 12.61. Found: C, 54.38; H, 3.71; N, 12.64.

**Ni(4,4'-dmbpy)(pyS)<sub>2</sub> (4b).** This complex was prepared in a manner analogous to that described for 4a. The yield was 3.3 g (93%). <sup>1</sup>H NMR (CDCl<sub>3</sub>, 20 °C): δ 110, 71.4, 58.4, 57.2, 10.7, 5.4, -9.2 ppm. Anal. Calcd for C<sub>22</sub>H<sub>20</sub>N<sub>4</sub>S<sub>2</sub>Ni·CH<sub>2</sub>Cl<sub>2</sub>: C, 50.39; H, 4.05; N, 10.22. Found: C, 50.35; H, 4.00; N, 10.18.

**Ni(4,4'-dmobpy)(pyS)<sub>2</sub> (4c).** This complex was prepared in a manner analogous to that described for 4a and recrystallized from a mixture of chloroform and hexane. The yield was 1.6 g (49%). <sup>1</sup>H NMR (CDCl<sub>3</sub>, 20 °C): δ 138, 111, 71.1, 56.9, 39.6 ppm. Anal. Calcd for C<sub>22</sub>H<sub>20</sub>N<sub>4</sub>S<sub>2</sub>O<sub>2</sub>Ni·0.25CHCl<sub>3</sub>: C, 50.89; H, 3.89; N, 10.67. Found: C, 50.93; H, 3.89; N, 10.54.

**Photolysis Setup for Hydrogen Evolution Studies.** Samples in EtOH/H<sub>2</sub>O (1/1; 5.0 mL) containing 4.0 μM catalyst, 2.0 mM Fl, and TEA (5% v/v) were prepared in 40 mL scintillation vials and protected from light before use. The pHs of the solutions were adjusted to pH 11.6 by adding HCl or NaOH and measured with a pH meter. The samples were placed into a temperature-controlled block at 15.0 °C and sealed with an airtight cap fitted with a pressure transducer and a septum. The samples were then degassed with 4/1 N<sub>2</sub>/CH<sub>4</sub> (1 atm), with the CH<sub>4</sub> being used later as an internal reference for GC analysis. The cells were irradiated from below with high-power Philips LumiLED Luxeon Star Hex green (520 nm) 700 mA LEDs. The light power density of each LED was set to 13 mW/cm<sup>2</sup> and measured with an L30 A Thermal sensor and Nova II power meter (Ophir-Spiricon LLC). The samples were swirled using an orbital shaker. The pressure changes in the vials were recorded using a Labview program from a Freesale semiconductor sensor (MPX4259A series). After irradiation, the headspace of the vials was sampled by GC to ensure that the pressure increases were due to H<sub>2</sub> evolution and to confirm the amount of H<sub>2</sub> evolved. The amounts of H<sub>2</sub> evolved were determined using a Shimadzu GC-17A gas chromatograph with a 5 Å molecular sieve column (30 m, 0.53 mm) and a TCD detector, by injecting 100 μL of headspace into the gas chromatograph, and were quantified by a calibration plot to the internal CH<sub>4</sub> standard.

**Cyclic Voltammetry.** Cyclic voltammetry (CV) measurements of the catalyst were performed with a CHI 680D potentiostat using a one-compartment cell with a glassy-carbon working electrode, a glassy-carbon auxiliary electrode, and an SCE reference electrode. The electrolyte for electrochemistry in 1/1 EtOH/H<sub>2</sub>O or MeOH/H<sub>2</sub>O was 0.1 M KNO<sub>3</sub> and in an 8/1/1 DMF/EtOH/H<sub>2</sub>O mixture was 0.1 M TBAPF<sub>6</sub>. Argon was used to purge all samples. In the acid concentration dependence study, a 2.0 M stock solution of acetic acid was prepared in the same solvent mixture with 0.1 M corresponding electrolyte. To a stirred and degassed 1.0 mM catalyst solution was added 5–10 μL of acid stock solution, and the mixture was purged with argon for another 300 s before performing cyclic voltammetry.

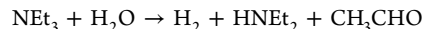
**Fluorescence Quenching.** A solution (3.0 mL) of Fl at 10 μM concentration in a 8/1/1 DMF/EtOH/H<sub>2</sub>O mixture (pH adjusted to 11.6) was prepared in a quartz cuvette fitted with a septum cap, and the solution was degassed under N<sub>2</sub> for 5 min. Aliquots of 30–100 μL of N<sub>2</sub>-degassed solution containing quencher and chromophore (10 μM) in the same solvent mixture (pH adjusted to 11.6) were added, and the intensity of the fluorescence was monitored by steady-state

fluorescence, exciting at 460 nm on a Spex Fluoromax-P fluorimeter with a photomultiplier tube detector.

**X-ray Diffraction Studies.** Crystals were placed onto the tips of glass capillary tubes or fibers and mounted on a Bruker SMART CCD platform diffractometer for data collection. For each crystal a preliminary set of cell constants and an orientation matrix were calculated from reflections harvested from three orthogonal wedges of reciprocal space. Full data collections were carried out using Mo Kα radiation (0.71073 Å, graphite monochromator) with frame times ranging from 25 to 60 s and at a detector distance of approximately 4 cm. Randomly oriented regions of reciprocal space were surveyed: three to six major sections of frames were collected with 0.50° steps in ω to three to six different φ settings and a detector position of -38° in 2θ. The intensity data were corrected for absorption.<sup>52</sup> Final cell constants were calculated from the xyz centroids of about 4000 strong reflections from the actual data collections after integration.<sup>53</sup>

Structures were solved using SIR97<sup>54</sup> and refined using SHELXL-97.<sup>55</sup> Space groups were determined on the basis of systematic absences, intensity statistics, or both. Direct-methods solutions were calculated, which provided most non-hydrogen atoms from the E map. Full-matrix least-squares/difference Fourier cycles were performed which located the remaining non-hydrogen atoms. All non-hydrogen atoms were refined with anisotropic displacement parameters. All hydrogen atoms were placed in ideal positions and refined as riding atoms with relative isotropic displacement parameters. Full-matrix least-squares refinements on F<sup>2</sup> were run to convergence.

**Systems with TEA as Sacrificial Donor.** When using TEA as a sacrificial donor, the net reaction being driven photochemically can be expressed by the equation



Using the tabulated thermochemical data,<sup>56</sup> the ΔH° value of this reaction is calculated to be +117.6 kJ/mol. If the entropy term is dominated by the release of H<sub>2</sub>, the ΔG° value for the reaction can be estimated to be +80 kJ/mol at 15 °C. Thus, it is a thermodynamically unfavorable reaction and must be driven by light energy.

## ■ ASSOCIATED CONTENT

### § Supporting Information

CIF files giving X-ray structures, tables giving crystal data and structure refinement details, and figures giving UV-vis and <sup>1</sup>H NMR spectra for nickel complexes, NMR spectra on 1a,d protonation, Fl fluorescence quenching data, cyclic voltammograms of nickel complexes with addition of acid in organic solvent, and additional photocatalytic hydrogen production data. This material is available free of charge via the Internet at <http://pubs.acs.org>.

## ■ AUTHOR INFORMATION

### Corresponding Author

\*Corresponding Authors [eisenberg@chem.rochester.edu](mailto:eisenberg@chem.rochester.edu); [patrick.holland@yale.edu](mailto:patrick.holland@yale.edu)

### Notes

The authors declare no competing financial interest.

## ■ ACKNOWLEDGMENTS

This work was supported by the Division of Chemical Sciences, Geosciences, and Biosciences, Office of Basic Energy Sciences, U.S. Department of Energy, Grant DE-FG02-09ER16121. We thank William McNamara for helpful discussions and Ryan Cowley for solving the crystal structure of complex 2.

## ■ REFERENCES

- (1) Lewis, N. S.; Nocera, D. G. *Proc. Natl. Acad. Sci. U.S.A.* **2006**, *103*, 15729.
- (2) Eisenberg, R. *Science* **2009**, *324*, 44.

- (3) Alstrum-Acevedo, J. H.; Brennaman, M. K.; Meyer, T. J. *Inorg. Chem.* **2005**, *44*, 6802.
- (4) Bard, A. J.; Fox, M. A. *Acc. Chem. Res.* **1995**, *28*, 141.
- (5) Esswein, A. J.; Nocera, D. G. *Chem. Rev.* **2007**, *107*, 4022.
- (6) Eckenhoff, W. T.; Eisenberg, R. *Dalton Trans.* **2012**, *41*, 13004.
- (7) Du, P. W.; Eisenberg, R. *Energy Environ. Sci.* **2012**, *5*, 6012.
- (8) Cline, E. D.; Adamson, S. E.; Bernhard, S. *Inorg. Chem.* **2008**, *47*, 10378.
- (9) Streich, D.; Astuti, Y.; Orlandi, M.; Schwartz, L.; Lomoth, R.; Hammarström, L.; Ott, S. *Chem. Eur. J.* **2010**, *16*, 60.
- (10) White, T. A.; Whitaker, B. N.; Brewer, K. J. *J. Am. Chem. Soc.* **2011**, *133*, 15332.
- (11) Han, Z.; Qiu, F.; Eisenberg, R.; Holland, P. L.; Krauss, T. D. *Science* **2012**, *338*, 1321.
- (12) Zhang, P.; Wang, M.; Dong, J. F.; Li, X. Q.; Wang, F.; Wu, L. Z.; Sun, L. C. *J. Phys. Chem. C* **2010**, *114*, 15868.
- (13) Fihri, A.; Artero, V.; Razavet, M.; Baffert, C.; Leibl, W.; Fontecave, M. *Angew. Chem., Int. Ed.* **2008**, *47*, 564.
- (14) Du, P. W.; Knowles, K.; Eisenberg, R. *J. Am. Chem. Soc.* **2008**, *130*, 12576.
- (15) Lazarides, T.; McCormick, T.; Du, P. W.; Luo, G. G.; Lindley, B.; Eisenberg, R. *J. Am. Chem. Soc.* **2009**, *131*, 9192.
- (16) McCormick, T. M.; Calitree, B. D.; Orchard, A.; Kraut, N. D.; Bright, F. V.; Detty, M. R.; Eisenberg, R. *J. Am. Chem. Soc.* **2010**, *132*, 15480.
- (17) Probst, B.; Rodenberg, A.; Guttentag, M.; Hamm, P.; Alberto, R. *Inorg. Chem.* **2010**, *49*, 6453.
- (18) Hawecker, J.; Lehn, J. M.; Ziessel, R. *Nouv. J. Chim.* **1983**, *7*, 271.
- (19) McCormick, T. M.; Han, Z. J.; Weinberg, D. J.; Brennessel, W. W.; Holland, P. L.; Eisenberg, R. *Inorg. Chem.* **2011**, *50*, 10660.
- (20) Rakowski DuBois, M.; DuBois, D. L. *Chem. Soc. Rev.* **2009**, *38*, 62.
- (21) Rakowski DuBois, M.; DuBois, D. L. *Acc. Chem. Res.* **2009**, *42*, 1974.
- (22) Helm, M. L.; Stewart, M. P.; Bullock, R. M.; Rakowski DuBois, M.; DuBois, D. L. *Science* **2011**, *333*, 863.
- (23) McLaughlin, M. P.; McCormick, T. M.; Eisenberg, R.; Holland, P. L. *Chem. Commun.* **2011**, *47*, 7989.
- (24) Zhang, W.; Hong, J.; Zheng, J.; Huang, Z.; Zhou, J. S.; Xu, R. J. *J. Am. Chem. Soc.* **2011**, *133*, 20680.
- (25) McNamara, W. R.; Han, Z.; Alperin, P. J.; Brennessel, W. W.; Holland, P. L.; Eisenberg, R. *J. Am. Chem. Soc.* **2011**, *133*, 15368.
- (26) McNamara, W. R.; Han, Z. J.; Yin, C. J.; Brennessel, W. W.; Holland, P. L.; Eisenberg, R. *Proc. Natl. Acad. Sci. U.S.A.* **2012**, *109*, 15594.
- (27) Singh, W. M.; Baine, T.; Kudo, S.; Tian, S. L.; Ma, X. A. N.; Zhou, H. Y.; DeYonker, N. J.; Pham, T. C.; Bollinger, J. C.; Baker, D. L.; Yan, B.; Webster, C. E.; Zhao, X. *Angew. Chem., Int. Ed.* **2012**, *51*, 5941.
- (28) Sun, Y.; Bigi, J. P.; Piro, N. A.; Tang, M. L.; Long, J. R.; Chang, C. J. *J. Am. Chem. Soc.* **2011**, *133*, 9212.
- (29) Sun, Y. J.; Sun, J. W.; Long, J. R.; Yang, P. D.; Chang, C. J. *Chem. Sci.* **2013**, *4*, 118.
- (30) Han, Z. J.; McNamara, W. R.; Eum, M. S.; Holland, P. L.; Eisenberg, R. *Angew. Chem., Int. Ed.* **2012**, *51*, 1667.
- (31) Bouwman, E.; Reedijk, J. *Coord. Chem. Rev.* **2005**, *249*, 1555.
- (32) Fontecilla-Camps, J. C.; Volbeda, A.; Cavazza, C.; Nicolet, Y. *Chem. Rev.* **2007**, *107*, 4273.
- (33) Tard, C.; Pickett, C. J. *Chem. Rev.* **2009**, *109*, 2245.
- (34) Cui, H. H.; Wang, J. Y.; Hu, M. Q.; Ma, C. B.; Wen, H. M.; Song, X. W.; Chen, C. N. *Dalton Trans.* **2013**, *42*, 8684.
- (35) Rosenfield, S. G.; Berends, H. P.; Gelmini, L.; Stephan, D. W.; Mascharak, P. K. *Inorg. Chem.* **1987**, *26*, 2792.
- (36) Schubert, E. M. *J. Chem. Educ.* **1992**, *69*, 62.
- (37) Lever, A. B. P. *Inorganic Electronic Spectroscopy*, 2nd ed.; Elsevier: Amsterdam, 1984; p 507.
- (38) Carroll, M. E.; Barton, B. E.; Rauchfuss, T. B.; Carroll, P. J. *J. Am. Chem. Soc.* **2012**, *134*, 18843.
- (39) Bard, A. J.; Faulkner, L. R. *Electrochemical Methods: Fundamentals and Applications*, 2nd ed.; Wiley: New York, 2001.
- (40) Lough, A. J.; Park, S.; Ramachandran, R.; Morris, R. H. *J. Am. Chem. Soc.* **1994**, *116*, 8356.
- (41) Petrou, A. L.; Koutselos, A. D.; Wahab, H. S.; Clegg, W.; Harrington, R. W.; Henderson, R. A. *Inorg. Chem.* **2011**, *50*, 847.
- (42) Fan, H. J.; Hall, M. B. *J. Am. Chem. Soc.* **2001**, *123*, 3828.
- (43) Ezzaher, S.; Capon, J. F.; Gloaguen, F.; Petillon, F. Y.; Schollhammer, P.; Talarmin, J.; Kervarec, N. *Inorg. Chem.* **2009**, *48*, 2.
- (44) Camara, J. M.; Rauchfuss, T. B. *J. Am. Chem. Soc.* **2011**, *133*, 8098.
- (45) Stewart, M. P.; Ho, M. H.; Wiese, S.; Lindstrom, M. L.; Thogerson, C. E.; Rauei, S.; Bullock, R. M.; Helm, M. L. *J. Am. Chem. Soc.* **2013**, *135*, 6033.
- (46) Wilson, A. D.; Newell, R. H.; McNevin, M. J.; Muckerman, J. T.; Rakowski DuBois, M.; DuBois, D. L. *J. Am. Chem. Soc.* **2006**, *128*, 358.
- (47) Wilson, A. D.; Shoemaker, R. K.; Miedaner, A.; Muckerman, J. T.; DuBois, D. L.; Rakowski DuBois, M. *Proc. Natl. Acad. Sci. U.S.A.* **2007**, *104*, 6951.
- (48) Pool, D. H.; DuBois, D. L. *J. Organomet. Chem.* **2009**, *694*, 2858.
- (49) Yang, J. Y.; Bullock, R. M.; Shaw, W. J.; Twamley, B.; Frazee, K.; Rakowski DuBois, M.; DuBois, D. L. *J. Am. Chem. Soc.* **2009**, *131*, 5935.
- (50) Hadadzadeh, H.; Mansouri, G.; Rezvani, A.; Khavasi, H. R.; Skelton, B. W.; Makha, M.; Charati, F. R. *Polyhedron* **2011**, *30*, 2535.
- (51) Castro, R.; Duran, M. L.; Garciaavazquez, J. A.; Romero, J.; Sousa, A.; Castineiras, A.; Hiller, W.; Strahle, J. J. *Chem. Soc., Dalton Trans.* **1990**, 531.
- (52) Sheldrick, G. M. *SADABS version 2008/1*; University of Göttingen, Göttingen, Germany, 2008.
- (53) *SAINT version 7.06A*; Bruker AXS, Madison, WI, 2003.
- (54) Altomare, A.; Burla, M. C.; Camalli, M.; Casciarano, G. L.; Giacovazzo, C.; Guagliardi, A.; Moliterni, A. G. G.; Polidori, G.; Spagna, R. *SIR97: A new program for solving and refining crystal structures*; Istituto di Cristallografia, CNR, Bari, Italy, 1999.
- (55) Sheldrick, G. M. *Acta Crystallogr., Sect. A* **2008**, *64*, 112.
- (56) *CRC Handbook of Chemistry and Physics*, 84th ed.; Lide, D. R., Ed.; CRC Press: Boca Raton, FL, 2003; Chapter 5.